Characterizations of Tropospheric Turbulence and Stability Layers From Aircraft Observations

John Y. N. Cho[1] and Reginald E. Newell

Department of Earth, Atmospheric, and Planetary Sciences, Massachusetts Institute of Technology, Cambridge, Massachusetts, USA

Bruce E. Anderson, John D. W. Barrick, and K. Lee Thornhill

NASA Langley Research Center, Hampton, Virginia, USA

Short title: TROPOSPHERIC TURBULENCE AND STABILITY LAYERS

[1]Now at Lincoln Laboratory, Massachusetts Institute of Technology, Lexington, Massachusetts, USA.

Abstract. Velocity, temperature, and specific humidity data collected by aircraft at 20-Hz resolution are analyzed for stability and turbulence parameters. Over 100 vertical profiles (mostly over the ocean) with a total of nearly 300 km in vertical airspace sampled are used. The compiled statistics show that anisotropy in the velocity fluctuations prevail down to the smallest spatial separations measured. A partitioning of convective versus dynamical instability indicates that in the free troposphere, the ratio of shear-produced turbulence to convectively produced turbulence increases from roughly 2:1 for weak turbulence ($\epsilon < 10^{-4}$ m^2 s^{-3}) to perhaps 3:1 for strong turbulence ($\epsilon > 10^{-4}$ m^2 s^{-3}). For the boundary layer, this ratio is close to 1:1 for weak turbulence and roughly 2:1 for strong turbulence. There is also a correlation between the strength of the vertical shear in horizontal winds and the turbulence intensity. In the free troposphere the turbulence intensity is independent of the degree of static stability, whereas in the boundary layer the turbulence intensity increases significantly with a fall in static stability. Vertical humidity gradients correlate with static stability in the free troposphere, which supports the basic notion that stable layers impede vertical mixing of trace gases and aerosols. In the boundary layer, however, this correlation does not hold. Vertical shear correlates with vertical humidity gradient, so it appears that the effect of differential advection creating tracer gradients wins out over differential advection destroying tracer gradients through shear-induced turbulence.

1. Introduction

Profiles of the Earth's atmosphere show varying degrees of stratification at a wide range of vertical scales. At large scales the stratification, as measured by the mean vertical temperature gradient, is used to define the major divisions of the neutral atmosphere: troposphere, stratosphere, mesosphere, and thermosphere. Zooming in to smaller scales, however, one discovers that embedded in each division are layers in which the sense of the temperature gradient is reversed. For example, the troposphere contains inversion layers through which the temperature increases with altitude, a kind of miniature stratosphere-within-a-troposphere phenomenon. If one goes to even smaller scales, then one observes reverses within the reverses, and so on to the limit of fluctuation dissipation by thermal diffusion.

Layers of static stability have important consequences for trace constituent distribution as can be clearly seen from the capping of the boundary layer. They also exist and play an important role in trace gas and aerosol distribution in the free troposphere [*Swap and Tyson*, 1999; *Cho et al.*, 2001; *Hobbs*, 2002]. At small thicknesses (of order 1 m or less) they are often called temperature sheets [*Dalaudier et al.*, 1994] and are of interest for their effects on radio and optical wave propagation.

Instability and turbulence also exist throughout the atmosphere. If they occur within statically stable regions, they exist as layers that can be as thin as several meters [e.g., *Muschinski and Wode*, 1998]. One school of thought ascribes the formation of temperature sheets to the action of such turbulent layers on the background temperature gradient (the "sheet and layer model"), with Kelvin-Helmholtz instability (KHI) as the generation mechanism [*Woods*, 1969]. Another theory invokes viscosity waves, not turbulence, as the creator of temperature sheets [*Hooke and Jones*, 1986; *Hocking et al.*, 1991].

Encounters with three-dimensional (3D) turbulence are thought to be the rapid, penultimate step in the vertical-scale cascade of atmospheric tracers, with the final

step, of course, being molecular diffusion. Because of the very anisotropic horizontal to vertical aspect ratio in the atmosphere, tracer filaments produced by large-scale differential advection are expected to be dissipated by processes acting along the vertical dimension [*Haynes and Anglade*, 1997].

Encounters with 3D turbulence at a more immediate "gut" level are events that aircraft passengers would like to avoid. Aside from turbulence due to convective storms, clear air turbulence (CAT) is invisible to the pilot and is difficult to forecast. KHI and breaking mountain waves are believed to the main culprits, and forecasting techniques have been developed for both of these turbulence generators [e.g., *Ellrod and Knapp*, 1992; *Bacmeister et al.*, 1994]. There has been recent evidence, however, of CAT arising from neither of these mechanisms [*Cho et al.*, 1999], and it has also been suggested that differential radiative heating by high-humidity layers might trigger instabilities [*Newell et al.*, 1999].

In this paper we analyze vertical profile data taken by the NASA P-3B aircraft during the Transport and Chemical Evolution Over the Pacific (TRACE-P) campaign. Horizontal and vertical velocity, temperature, and specific humidity effectively sampled at 20 Hz are used to compile statistics on various stability and turbulence parameters. Using these statistics, we examine the following questions: What is the probability distribution of the turbulence energy dissipation rate ϵ? What are the relative contributions of dynamical versus convective instability to turbulence generation? Do high-humidity layers contribute to CAT? How efficiently does 3D turbulence destroy vertical gradients in tracers? How do the answers to the above questions differ for the boundary layer versus the free troposphere?

2. Experiment Description

TRACE-P, which took place during February–April 2001, was the latest in the line of NASA Global Tropospheric Experiment (GTE) aircraft missions [*McNeal et al.*,

1983] conducted to study atmospheric chemistry. This campaign focused on evaluating the outflow of chemically and radiatively important gases and aerosols from the Asian continent, and, as such, was staged in the western Pacific. For an overview of the mission with flight track maps, instrument lists, etc., see Jacob et al., The TRACE-P experiment: Objectives, design, and execution, to be submitted to *J. Geophys. Res.* A detailed summary of the meteorological conditions is given by Fuelberg et al., A meteorological overview of the TRACE-P period, to be submitted to *J. Geophys. Res.*

Two aircraft, a DC-8 and a P-3B, were used during TRACE-P. This study will utilize data from the P-3B, because it was equipped with a turbulent air motion measurment system (TAMMS) that had an effective sampling rate of 20 Hz. The turboprop P-3B had a ceiling of 8 km and was mainly used for sampling the boundary layer up to mid-tropospheric heights. The DC-8 with its higher ceiling covered the upper troposphere and lower stratosphere, but it was not equipped with a turbulence measurement system. Typical flight patterns for the P-3B consisted of level segments at different altitudes connected by steep ascents and descents. Since we are interested in vertical gradient quantities, we will extract profile data provided by these up- and down-legs.

For a detailed description of the TAMMS, see *Considine et al.* [1999]. Calibration procedures were outlined in *Barrick et al.* [1996].

3. Data Analysis Issues

The TAMMS took data during flights 4 through 24. The primary inertial navigation system (used to calculate the wind components), however, was turned off during flights 4, 11, and 24, so we did not include data from those flights. The Lyman-α hygrometer was not operating properly during flights 19 and 21, so we also omitted those flights. In the remaining 16 flights, there were 184 profiles of vertical extent longer than 1000 m. We carefully went through each of these profiles and looked at the velocity, temperature,

and specific humidity data. If there was a data gap or glitch in any of those measured parameters, we eliminated that profile from consideration. We also examined the Fourier power spectra of the velocity data and discarded profiles that appeared to have the noise floor exceeding the signal level at the highest frequencies; this occurred occasionally for the vertical velocity spectra. This was done in order to assure valid estimates of ϵ. The resulting statistics on turbulence, however, could be somewhat biased against the quietest conditions because of this procedure. Being quite conservative in the quality control step, we were left with 106 profile segments for a total of 296 km of vertically sampled airspace. We also used changes in temperature, humidity, and velocity with height to mark the approximate altitude of the top of the boundary layer if the profile crossed over such a border.

When we write "vertical profile," it is, of course, not literally correct for fixed-wing aircraft data. For the P-3B, which typically flies at $\sim$150 m s^{-1} and ascends/descends at $\sim$5 m s^{-1}, the slope is about 30:1. However, the aspect ratio of the large-scale atmosphere is much larger, roughly suggested by the inverse of Prandtl's ratio f/N, where f is the Coriolis parameter and N is the Brunt-Väisälä frequency [*Charney*, 1971]. For the midlatitude troposphere this ratio is about 120:1. Inside convective storms and regions of 3D turbulence, this scaling does not hold. For scales inside or smaller than the inertial range of turbulence, fluctuating quantities tend toward isotropy, although there is ongoing debate about how isotropic turbulence can be inside a real stratified shear flow even at these small scales [e.g., *Smyth and Moum*, 2000]. The outer scale of turbulence depends on ϵ and N [*Weinstock*, 1978], but a reasonable free tropospheric value seems to be $\sim$100 m [e.g., *Cho et al.*, 1999]. The "vertical profile" approximation should hold for Δz quantities greater than the turbulence outer scale, where Δz is the difference in altitude of two points.

To calculate ϵ, we followed the procedure adopted by *Meischner et al.* [2001]. The second-order structure functions for u, v, and w (the zonal, meridional, and vertical

velocity components) were computed directly from the 20-Hz time series. In the time domain, the second-order structure function for zonal velocity is given by

$$D_{uu}(\Delta t) = \left\langle [u(t+\Delta t) - u(t)]^2 \right\rangle \tag{1}$$

where Δt is the chosen time increment over which to take the difference. For the meridional and vertical components, simply replace the us with vs and ws. For sufficiently small Δt, the aircraft travels in a straight line, so the structure functions can be easily transformed from the temporal to the spatial domain using the airspeed U_a by letting $\Delta t = r/U_a$, where r is the spatial separation between the differenced points.

For locally isotropic turbulence, ϵ can be calculated from $D_{TT} = 4C(\epsilon r)^{2/3}/3$ [*Monin and Yaglom*, 1975], where D_{TT} is the transverse (velocity component normal to the flight direction) structure function and C is a constant. We will use $C = 2.05$ [*Panofsky and Dutton*, 1984; *Paluch and Baumgartner*, 1989]. For purely horizontal flights, which is not a bad assumption considering our gradual ascent/descent slopes, $D_{TT} = D_{ww}$, so it is possible to estimate ϵ from w only. However, we can also include the other components, since there is a horizontal transverse direction, which may improve the statistical accuracy. Since $D_{uu} + D_{vv} = 7D_{TT}/4$ for isotropic turbulence, an equal weighting of the three orthogonal components yields [*Meischner et al.*, 2001]

$$D_{TT} = \frac{1}{3}\left[\frac{8}{7}\left(D_{uu} + D_{vv}\right) + D_{ww}\right] . \tag{2}$$

We also computed a ratio $I = (7/4)[D_{ww}/(D_{uu} + D_{vv})]$, which should be unity for isotropy. If $I < 1$, then there is more energy in the horizontal motions than in the vertical motions (the expected case for large-scale flow). This ratio, then, should increase from a small fraction toward 1 as the r used in the calculation decreases into inertial subrange scales.

To calculate the vertical gradient quantities, we first interpolated the data onto a uniform 1-m altitude spacing. Then we simply took the difference in the quantity

divided by a chosen Δz. We calculated the square of the vertical shear in horizontal winds, $(dU/dz)^2 = [(u(z+\Delta z) - u(z))^2 + (v(z+\Delta z) - v(z))^2]/(\Delta z)^2$; the vertical gradient of specific humidity squared, $(dq/dz)^2 = [q(z+\Delta z) - q(z)]^2/(\Delta z)^2$; the Brunt-Väisälä frequency squared, $N^2 = (g/\bar{\theta})[\theta(z+\Delta z) - \theta(z)]/\Delta z$, where g is the gravitational acceleration, θ is the potential temperature, and $\bar{\theta}$ is the mean potential temperature; and the gradient Richardson number, $Ri = N^2/(dU/dz)^2$. Also, in order to assess the thermodynamic effects of humidity on stability, we computed N_v^2 and Ri_v where the differenced θ quantities are replaced by the virtual potential temperature θ_v for unsaturated conditions and by the equivalent potential temperature θ_e for saturated conditions.

For statistics comparing ϵ and I to the gradient quantities, we interpolated ϵ and I to the same 1-m altitude grid used above in order to have exact coincidence.

4. Discussion of Results

4.1. Single-Parameter PDFs

Figure 1.

Figure 1 indicates the locations of the vertical profiles used in this paper. One sees that virtually all of the data were taken over water. Figure 2d gives the probability distribution function (PDF) of the number of data points used with respect to latitude. The PDFs in Figures 2a to c are divided into the free troposphere (solid lines) and the boundary layer (dashed lines). One can see that most of the data points were taken in the lower to midtroposphere. The relative humidity PDFs show a very dry mode for the free troposphere (but with a non-negligible tail at wet values) and a very wet mode for the boundary layer (not surprising since almost all the profiles were over water). The fat tail in the free tropospheric relative humidity PDF should give us a significant amount of data with which to examine the potential effect of humidity on CAT generation.

Figure 2.

Before we go on to discuss the statistics, let us look at an example profile. Figure 3

Figure 3.

shows the vertical profiles of temperature (T), q, N^2, $(dU/dz)^2$, and $\log \epsilon$. For vertical gradient quantities $\Delta z = 100$ m was used. For the ϵ calculation $\Delta t = 0.05$ s was used. The vertical lines at $\log \epsilon = -3$ indicate heights where $Ri \leq 1/4$, i.e., potentially unstable layers. There are a few interesting features to note. The high-humidity layer between ~2 km and ~2.7 km is bounded by layers of strong static stability (temperature inversions) and shear. This morphology suggests large-scale differential advection creating a distinct tracer layer. Whether the high static stability at its edges was also a result of the differential advection or the preexisting stability layers forced the differential advection is an open question. The high-humidity layer is also turbulent, with the $Ri < 1/4$ condition created by low or negative values of N^2. Perhaps as a result of the eddy mixing the layer appears well mixed, whereas there are sharp gradients in q at the stable edges. One wonders whether the high humidity contributed to the creation of a statically unstable environment within the layer. (The relative humidity in this layer was significantly below saturation, so it was probably not cloudy.) However, one can also see that the regions of potential instability as delineated by $Ri \leq 1/4$ does not always coincide with turbulent layers in other sections of this profile.

The turbulent layer from ~3.8 km to ~4.2 km is also bounded by regions of high static stability and strong shear. Ozone (peaking at ~140 ppbv) and carbon monoxide measurements (not shown here) indicate that this layer came from the stratosphere, probably through a tropopause fold. Again, differential advection is indicated, but this time the layer is too dry to support the idea that humidity might have been the cause of the convective instability. It is even more puzzling because stratospheric air intruding into the troposphere tends to be more statically stable than the surrounding air.

Let us now move on to the statistical results. Figures 4a and b display the PDFs of $\log \epsilon$ for the free troposphere and boundary layer. Values of $\Delta t = 0.05$ s (solid), 0.25 s (dashed), and 0.5 s (dash-dotted) were used. For a nominal airspeed of 150 m s^{-1}, these Δt values correspond to separations of $r = 7.5$, 37.5, and 75 m. Note the bimodal

Figure 4.

distribution for the boundary layer, clearly indicating a separation between calm and turbulent conditions. The demarcation seems to occur at $\epsilon \sim 10^{-5}$ m^2 s^{-3}. The free tropospheric PDFs have a single mode at very low values of ϵ and monotonically decreases with strength. This shows the very intermittent nature of turbulence outside of the boundary layer. The PDFs shift slightly to larger values with increasing Δt used in the calculation, which simply means that the assumption of local isotropy used in the formula does not always hold in the measured real world. Otherwise the calculated ϵ should not depend on Δt.

The anisotropy can be more clearly observed in Figures 4c and d. In general, $I < 1$ ($\log I < 0$), and there is a tendency for the PDFs to slide to lower values with increasing Δt, which is expected—the anisotropy should increase with scale. What is surprising is how few values are close to true isotropy. True, most of the data in the free troposphere were taken under calm conditions, but even for the boundary layer, where turbulent conditions were more prevalent, there were not many data points where $I \sim 1$.

The mean, median, log-mean, and mode values from the above PDFs are collected in Tables 1 and 2. The boundary layer is clearly more turbulent and closer to isotropy (at the examined scales) than the free troposphere. The tendencies with respect to Δt apparent in the PDFs can also be discerned in these average values. Because the $\Delta t = 0.05$ s output come closest to the approximation of a locally isotropic inertial subrange, we will use only those results in the rest of the paper.

Table 1.

Table 2.

Let us now examine the statistics of the vertical gradient quantities. Figures 4e and f show the PDFs of $\log(dq/dz)^2$ for $\Delta z = 10$ m (solid), 100 m (dashed), and 1000 m (dash-dotted) in the free troposphere and boundary layer. Again, as expected, the gradients become weaker with increasing Δz. We also see that $(dq/dz)^2$ is close to a log-normal distribution, at least for $\Delta z = 10$ m. The various average values of the PDFs are given in Tables 3 and 4. The specific humidity gradients are stronger in the boundary layer than in the free troposphere at all scales. This implies that even

Table 3.

Table 4.

though the mixing is more vigorous in the boundary layer, the background gradient generated by having the water vapor source at the surface and the sink at the top wins out over the homogenizing effect of turbulence. The generally higher values of q in the boundary layer also contributes to this difference since the gradients were not computed as fractional changes in specific humidity.

The PDFs of the vertical shear in horizontal winds are displayed in Figures 5a and b. Again, $(dU/dz)^2$ appears to be log-normally distributed, and the values decreasing with increasing Δz. Average quantities are listed in Tables 3 and 4. **Figure 5.**

The PDFs of N^2 shown in Figures 5c and d indicate a tendency to shift to lower values with increasing Δz. However, if one only looks at the mean values this would not be apparent (Tables 5 and 6). This tendency is most apparent in the mode values. Perhaps a more physically relevant parameter for turbulence is the percentage of data with $N^2 \leq 0$ values, which indicates a convectively unstable situation. Table 7 lists these values. Note the strong dependency of this parameter on Δz. We also see that the boundary layer is generally more convectively unstable than the free troposphere. **Table 5.** **Table 6.** **Table 7.**

We can combine the shear and static stability measures to get Ri. The PDFs are shown in Figures 5e and f. There is a strong dependence on Δz, which is clearly displayed in Tables 8 and 9. Again, the critical parameter is the percentage of data with $Ri \leq 1/4$ values, and these are tabulated in Table 10. Do these numbers imply that more than half of 10-m layers were potentially unstable? Not necessarily. As discussed earlier, the concept of "vertical profile" at 10-m may not be valid, and also the signals at these small scales may include a great deal of statistical noise. In terms of the use of these gradient quantities as a background against which turbulence might be generated, the $\Delta z = 100$ m values are probably most reasonable. The location of the modes of the Ri PDFs close to 1/4 for $\Delta z = 100$ m also supports this proposition, since convective adjustment of the atmosphere may tend to "pile up" Ri numbers near the critical value for scales within the typical outer scale of turbulence. **Table 8.** **Table 9.** **Table 10.**

We can compare the N^2 and Ri results with those of N_v^2 and Ri_v. The latter quantities include the thermodynamic effects of water vapor on static stability. The PDFs are plotted in Figure 6 and the average quantities listed in Tables 5 through 10. The effects are negligible in the free troposphere, but even in the boundary layer the effects are quite small, providing only slightly more potential instability in the atmosphere. We will go ahead and use N_v^2 and Ri_v instead of N^2 and Ri in the rest of the paper in order to include the effects of water vapor.

Figure 6.

4.2. Parameter Dependencies

In order to study the dependence of one parameter on another, we computed joint PDFs for pairs of variables. The $\Delta z = 100$ m quantities were used for the vertical gradient parameters, since we saw that this thickness was probably most reasonable to assume for the turbulence outer scale. As stated before, the $\Delta t = 0.05$ s results were used for ϵ and I. Although we tried plotting the full two-dimensional PDFs on a color scale, we found that the results were clearer to the eye if we simply graphed the median values of one variable against the values of the other variable. Figure 7a shows the dependency of the isotropy ratio I on ϵ. For $\epsilon > 10^{-6}$ m^2 s^{-3} I increased with ϵ, which is consistent with the usual assumption that fully developed turbulence is more isotropic than weak or no turbulence. The reversal of the trend for $\epsilon < 10^{-6}$ m^2 s^{-3} probably indicates that the velocity fluctuations were disappearing below the instrumental noise floor at these levels. (Presumably instrumental noise would be more isotropic than the atmospheric fluctuations.) Note that the trends were almost exactly the same for the free troposphere (solid line) and the boundary layer (dashed line), implying a universality to this dependency.

Figure 7.

Figure 7b shows that for $\epsilon > 10^{-6}$ m^2 s^{-3}, ϵ increased with shear. This trend seems to increase at the largest ϵ values. This dependency suggests that shear instability is a key controller of turbulence intensity, both in the free troposphere and the boundary

layer.

In contrast we have Figure 8a, which suggests that static stability has a marked influence on turbulence intensity in the boundary layer but not in the free troposphere. Note the independence of N_v^2 and ϵ in the free troposphere, whereas in the boundary layer N_v^2 decreases with ϵ for large ϵ values. There is a sharp transition at ϵ somewhat above 10^{-5} m^2 s^{-3}, which corresponds to the dip in the bimodal PDF observed in Figure 4b. The mainly marine boundary layers that we sampled could clearly be divided into calm, stable conditions and turbulent conditions. The percentage of data with $N_v^2 \leq 0$ vs. $\log \epsilon$ is graphed in Figure 8c, showing again the importance of statically unstable conditions for turbulence production in the boundary layer.

Figure 8.

In an attempt to differentiate between the contributions of shear vs. convective instabilities to turbulence generation, we calculated the percentage of data with $Ri_v \leq 0$ and $0 < Ri_v \leq 1/4$. The former includes all convectively unstable situations, while the latter includes only (potentially) dynamically unstable conditions. The results are plotted in Figures 9a and b. In the free troposphere, the ratio of shear-produced turbulence to convectively produced turbulence increases from roughly 2:1 for weak turbulence ($\epsilon < 10^{-4}$ m^2 s^{-3}) to perhaps 3:1 for strong turbulence ($\epsilon > 10^{-4}$ m^2 s^{-3}). For the boundary layer, this ratio is close to 1:1 for weak turbulence and roughly 2:1 for strong turbulence.

Figure 9.

It is of interest to note that shear and static stability are not statistically independent. In fact, Figure 7f clearly shows that for a statically stable environment, shear and static stability are positively correlated. This dependency further sharpens the division between dynamically unstable and convectively unstable conditions.

Finally we examine the relationship of the vertical gradient in specific humidity to the other variables. The motivation was to see if statistically we could discern the types of correlations we noted in Figure 3 between gradients in a tracer (specific humidity) and turbulence or static stability. From simple physical reasoning we might expect that

strong tracer gradients would be correlated with statically stable layers and that weak gradients would be correlated with the smoothing effects of turbulent layers. (Strong humidity gradients can also cause differential radiative heating/cooling, which could indirectly affect the static stability.)

Results exhibited in Figures 7c and e indicate that vertical humidity gradients are not strongly affected by turbulence. Figure 7d shows some positive correlation between shear and tracer gradient, which suggests differential advection as a key player in generating vertical tracer gradients. Static stability also increased with $(dq/dz)^2$ for strong humidity gradients in the free troposphere (Figure 8b), which validates the idea that static stability impedes vertical mixing of tracer layers. This is, however, not true in the boundary layer; there, $(dq/dz)^2$ is independent of N_v^2 except for very strong humidity gradients, where the two variables are anticorrelated. This somewhat counterintuitive result may be due to the fact that there is a source of water vapor at the surface and convectively unstable conditions may produce fairly small-scale horizontal inhomogeneities (e.g., convective towers) that can get aliased into the measured vertical gradients. The percentage of data with $N_v^2 \leq 0$ does seem to decrease with increasing $(dq/dz)^2$ in the mid-range of humidity gradient values (Figure 8d), and this is weakly reflected in the percentages of data with Ri_v below the critical thresholds (Figures 9c and d). This lack of a strong tendency may be the result of two offsetting factors: Ri_v is lowered by increased shear and becomes negative when N_v^2 goes negative, but while the former is associated with increased $(dq/dz)^2$ (Figure 7d), the latter condition is associated with decreased $(dq/dz)^2$.

5. Conclusions

The data set used for this study is not necessarily representative of the global troposphere. Almost all the profiles were flown over the ocean, the latitudinal coverage was limited to between 15°N and 45°N, and the maximum height was less than 8 km.

However, there were 106 vertical profiles used with a total of nearly 300 km in vertical airspace sampled. The 20-Hz resolution provided a wide range of spatial scales to examine. The PDFs calculated for the various quantities were reasonably well-behaved, and certain patterns and trends emerged that appeared to have physical significance.

First, the PDFs of $\log \epsilon$ had very different forms for the free troposphere and the boundary layer. For the former, the PDF was unimodal with the peak at $\sim 10^{-6}$ m^2 s^{-3} and a fat tail extending to higher values. For the latter, the PDF was bimodal with a similar "calm" peak and a higher "turbulent" peak at $\sim 10^{-4}$ m^2 s^{-3}. The implication is that the (marine) boundary layer is populated by distinct laminar and turbulent flow conditions and that the latter condition is more prevalent. In the free troposphere, on the other hand, the background "basic" state is calm and turbulence occurs only intermittently.

Second, the PDFs of the isotropy ratio I showed that anisotropy (horizontal velocity flutuations greater than vertical velocity fluctuations) prevailed even down to the limit of spatial resolution ($\sim$8 m). This was true even for the boundary layer where turbulent conditions were common. However, the degree of isotropy did increase with decreasing scale as expected, and the boundary layer velocity fluctuations were more isotropic than the free tropospheric fluctuations.

Third, we estimated that in the free troposphere, the ratio of shear-produced turbulence to convectively produced turbulence increased from roughly 2:1 for weak turbulence ($\epsilon < 10^{-4}$ m^2 s^{-3}) to perhaps 3:1 for strong turbulence ($\epsilon > 10^{-4}$ m^2 s^{-3}). For the boundary layer, this ratio was close to 1:1 for weak turbulence and roughly 2:1 for strong turbulence. We also noted a correlation between the strength of the vertical shear in horizontal winds and the turbulence intensity. In the free troposphere the turbulence intensity seemed to be independent of the degree of static stability, whereas in the boundary layer the turbulence intensity increased significantly with a fall in static stability.

Fourth, the thermodynamic effect of water vapor on static stability was negligible in the free troposphere. This effect was noticeable but still small in the boundary layer. We must note, however, that the flights on this mission tended to avoid areas of clouds because of certain objectives set by the chemistry program. Also, the season was late winter to early spring when the sea surface temperatures were low. We cannot rule out an influence of water vapor on the static stability of layers through differential radiative heating/cooling from these results—that type of study is outside the scope of this paper.

Finally, vertical humidity gradients did correlate statistically with static stability in the free troposphere, which supports the basic notion that stable layers impede vertical mixing of trace gases and aerosols. In the boundary layer, however, this correlation did not hold; in fact, the reverse was true for very strong gradients. This suggests that the strong humidity gradients in the marine boundary layer were not mainly generated by stable conditions but by convective turbulence; perhaps small-scale horizontal inhomogeneities created by convective cells or towers were aliased into the "vertical" profiles. Vertical shear correlated with vertical humidity gradient, so it appears that the effect of differential advection creating tracer gradients won out over differential advection destroying tracer gradients through KHI-induced turbulence on average.

Acknowledgments. The MIT work was funded by NASA grants NCC1-415 and NAG1-2306. We wish to thank Donald Bagwell for putting together the TAMMS data acquisition system and providing programming support.

References

Bacmeister, J. T., P. A. Newman, B. L. Gary, and K. R. Chan, An algorithm for forecasting mountain wave-related turbulence in the stratosphere, *Wea. Forecasting*, *9*, 241–253, 1994.

Barrick, J. D. W., J. A. Ritter, C. E. Watson, M. W. Wynkoop, J. K. Quinn, and D. R. Norfolk, Calibration of NASA turbulent air motion measurement system, *NASA Tech. Pap. TP-3610*, 1996.

Charney, J. G., Geostrophic turbulence, *J. Atmos. Sci.*, *28*, 1087–1095, 1971.

Cho, J. Y. N., R. E. Newell, E. V. Browell, W. B. Grant, C. F. Butler, and M. A. Fenn, Observation of pollution plume capping by a tropopause fold, *Geophys. Res. Lett.*, *28*, 3243–3246, 2001.

Cho, J. Y. N., et al., Observations of convective and dynamical instabilities in tropopause folds and their contribution to stratosphere-troposphere exchange, *J. Geophys. Res.*, *104*, 21,549–21,568, 1999.

Considine, G. D., B. Anderson, J. Barrick, and D. H. Lenschow, Characterization of turbulent transport in the marine boundary layer during flight 7 of PEM-Tropics A, *J. Geophys. Res.*, *104*, 5855–5863, 1999.

Dalaudier, F., C. Sidi, M. Crochet, and J. Vernin, Direct evidence of "sheets" in the atmospheric temperature field, *J. Atmos. Sci.*, *51*, 237–248, 1994.

Ellrod, G. P., and D. I. Knapp, An objective clear-air turbulence forecasting technique: Verification and operational use, *Wea. Forecasting*, 7, 150–165, 1992.

Haynes, P., and J. Anglade, The vertical-scale cascade in atmospheric tracers due to large-scale differential advection, *J. Atmos. Sci.*, *54*, 1121–1136, 1997.

Hobbs, P. V., Clean air slots amid atmospheric pollution, *Nature*, *415*, 861, 2002.

Hocking, W. K., S. Fukao, M. Yamamoto, T. Tsuda, and S. Kato, Viscosity waves and thermal-conduction waves as a cause of "specular" reflectors in radar studies of the atmosphere, *Radio Sci.*, *26*, 1281–1303, 1991.

Hooke, W. H., and R. M. Jones, Dissipative waves excited by gravity-wave encounters with the stably stratified planetary boundary layer, *J. Atmos. Sci.*, *43*, 2048–2060, 1986.

McNeal, R. J., J. P. Mugler Jr., R. C. Harriss, and J. M. Hoell Jr., NASA Global Tropospheric Experiment, *Eos Trans. AGU*, *64*, 561–562, 1983.

Meischner, P., R. Baumann, H. Höller, and T. Jank, Eddy dissipation rates in thunderstorms estimated by Doppler radar in relation to aircraft in situ measurements, *J. Atmos. Oceanic Technol.*, *18*, 1609–1627, 2001.

Monin, A. S., and A. M. Yaglom, *Statistical Fluid Mechanics: Mechanics of Turbulence*, vol. 2, 874 pp., MIT Press, Cambridge, Mass., 1975.

Muschinski, A., and C. Wode, First in-situ evidence for co-existing sub-meter temperature and humidity sheets in the lower free troposphere, *J. Atmos. Sci.*, *55*, 2893–2906, 1998.

Newell, R. E., V. Thouret, J. Y. N. Cho, P. Stoller, A. Marenco, and H. G. Smit, Ubiquity of quasi-horizontal layers in the troposphere, *Nature*, *398*, 316–319, 1999.

Paluch, I. R., and D. G. Baumgartner, Entrainment and fine-scale mixing in a continental convective cloud, *J. Atmos. Sci.*, *46*, 261–278, 1989.

Panofsky, H. A., and J. A. Dutton, *Atmospheric Turbulence*, 397 pp., J. Wiley and Sons, New York, 1984.

Smyth, W. D., and J. N. Moum, Anisotropy of turbulence in stably stratified mixing layers, *Phys. Fluids*, *12*, 1343–1362, 2000.

Swap, R. J., and P. D. Tyson, Stable discontinuities as determinants of the vertical distribution of aerosols and trace gases in the atmosphere, *S. Afr. J. Sci.*, *95*, 63–71, 1999.

Weinstock, J., On the theory of turbulence in the buoyancy subrange of stably stratified flows, *J. Atmos. Sci.*, *35*, 634–649, 1978.

Woods, J. D., On Richardson's number as a criterion for laminar-turbulent-laminar transition in the ocean and atmosphere, *Radio Sci.*, *4*, 1289–1298, 1969.

B. E. Anderson, J. D. W. Barrick, and K. L. Thornhill, Mail Stop 483, NASA Langley Research Center, 21 Langley Boulevard, Hampton, VA 23681-2199, USA. (b.e.anderson@larc.nasa.gov; j.d.barrick@larc.nasa.gov; k.l.thornhill@larc.nasa.gov)

J. Y. N. Cho, Lincoln Laboratory, M.I.T., 244 Wood Street, Lexington, MA 02420-9108, USA. (jync@mit.edu)

R. E. Newell, Department of Earth, Atmospheric, and Planetary Sciences, M.I.T., 77 Massachusetts Ave., #54-1824, Cambridge, MA 02139-4307, USA. (renewell@mit.edu)

Received _____

This manuscript was prepared with AGU's LaTeX macros v4, with the extension package 'AGU++' by P. W. Daly, version 1.6b from 1999/08/19.

Figure Captions

Figure 1. Locations of the vertical profiles used in this paper marked by crosses.

Figure 2. Probability distribution functions of the number of data points with respect to (a) altitude, (b) relative humidity, (c) potential temperature, and (d) latitude. For (a) through (c) the solid line represents the free troposphere and the dashed line denotes the boundary layer.

Figure 3. Vertical profile taken at 30°N, 131°E, on March 31, 2001, around 0430 UT. The vertical lines at $\log \epsilon = -3$ indicate heights where $Ri \leq 1/4$.

Figure 4. PDFs of $\log \epsilon$ and $\log I$ for $\Delta t = 0.05$ s (solid), 0.25 s (dashed), and 0.5 s (dash-dotted). Also PDFs of $\log(dq/dz)^2$ for $\Delta z = 10$ m (solid), 100 m (dashed), and 1000 m (dash-dotted). The left-hand column is for free tropospheric data and the right-hand column is for boundary layer data.

Figure 5. PDFs of $\log(dU/dz)^2$, N^2, and Ri for $\Delta z = 10$ m (solid), 100 m (dashed), and 1000 m (dash-dotted). The left-hand column is for free tropospheric data and the right-hand column is for boundary layer data. The vertical lines in (c) and (d) mark $N^2 = 0$. The vertical lines in (e) and (f) mark the critical $Ri = 1/4$ level.

Figure 6. PDFs of N_v^2 and Ri_v for $\Delta z = 10$ m (solid), 100 m (dashed), and 1000 m (dash-dotted). The left-hand column is for free tropospheric data and the right-hand column is for boundary layer data. The vertical lines in (a) and (b) mark $N_v^2 = 0$. The vertical lines in (c) and (d) mark the critical $Ri_v = 1/4$ level.

Figure 7. Plots of (a) the median of $\log I$ vs. $\log \epsilon$, (b) the median of $\log(dU/dz)^2$ vs. $\log \epsilon$, (c) the median of $\log I$ vs. $\log(dq/dz)^2$, (d) the median of $\log(dU/dz)^2$ vs. $\log(dq/dz)^2$, (e) the median of $\log \epsilon$ vs. $\log(dq/dz)^2$, and (f) the median of $\log(dU/dz)^2$ vs. N_v^2. Solid lines denote free tropospheric data, and dashed lines denote boundary layer data.

Figure 8. Plots of (a) the median of N_v^2 vs. $\log \epsilon$, (b) the median of N_v^2 vs. $\log(dq/dz)^2$, (c) the percentage of data with $N_v^2 \leq 0$ vs. $\log \epsilon$, and (d) the percentage of data with $N_v^2 \leq 0$ vs. $\log(dq/dz)^2$. Solid lines denote free tropospheric data, and dashed lines denote boundary layer data.

Figure 9. Percentage of data with (solid) $Ri_v \leq 0$ and (dashed) $0 < Ri_v \leq 1/4$. (a) and (b) are plotted against $\log \epsilon$, while (c) and (d) are plotted against $\log(dq/dz)^2$. The free tropospheric cases are in the left-hand column and the boundary layer cases are in the right-hand column.

Tables

Table 1. Turbulence Parameters in the Free Troposphere

Parameter	ϵ, m^2 s^{-3}			I		
Δt, s	0.05	0.25	0.5	0.05	0.25	0.5
Mean	2.4×10^{-5}	5.1×10^{-5}	5.7×10^{-5}	0.21	0.19	0.22
Median	1.5×10^{-6}	2.5×10^{-6}	2.9×10^{-6}	0.17	0.12	0.13
Log-Mean	2.7×10^{-6}	4.2×10^{-6}	4.3×10^{-6}	0.18	0.13	0.13
Mode	8.9×10^{-7}	1.3×10^{-6}	1.4×10^{-6}	0.16	0.11	0.13

Table 2. Turbulence Parameters in the Boundary Layer

Parameter	ϵ, m^2 s^{-3}			I		
Δt, s	0.05	0.25	0.5	0.05	0.25	0.5
Mean	2.7×10^{-4}	6.2×10^{-4}	7.3×10^{-4}	0.32	0.36	0.38
Median	5.1×10^{-5}	1.0×10^{-4}	1.1×10^{-4}	0.29	0.28	0.26
Log-Mean	3.9×10^{-5}	7.7×10^{-5}	8.5×10^{-5}	0.27	0.26	0.25
Mode	1.4×10^{-4}	2.5×10^{-4}	2.0×10^{-4}	0.35	0.32	0.32

Table 3. Vertical Gradient Parameters in the Free Troposphere

Parameter	$(dU/dz)^2$, s^{-2}			$(dq/dz)^2$, $g^2\ kg^{-2}\ m^{-2}$		
Δz, m	10	100	1000	10	100	1000
Mean	1.9×10^{-3}	2.4×10^{-4}	5.1×10^{-5}	5.9×10^{-4}	7.6×10^{-5}	1.2×10^{-5}
Median	5.3×10^{-4}	1.1×10^{-4}	3.2×10^{-5}	1.2×10^{-5}	4.1×10^{-6}	2.2×10^{-6}
Log-Mean	5.0×10^{-4}	9.6×10^{-5}	2.6×10^{-5}	9.5×10^{-6}	2.9×10^{-6}	1.0×10^{-6}
Mode	5.0×10^{-4}	1.3×10^{-4}	4.0×10^{-5}	1.6×10^{-5}	1.3×10^{-5}	6.3×10^{-6}

Table 4. Vertical Gradient Parameters in the Boundary Layer

Parameter	$(dU/dz)^2$, s^{-2}			$(dq/dz)^2$, $g^2\ kg^{-2}\ m^{-2}$		
Δz, m	10	100	1000	10	100	1000
Mean	1.8×10^{-2}	4.4×10^{-4}	6.4×10^{-5}	5.3×10^{-3}	3.2×10^{-4}	3.0×10^{-5}
Median	2.8×10^{-3}	1.7×10^{-4}	3.8×10^{-5}	8.4×10^{-5}	1.9×10^{-5}	1.3×10^{-5}
Log-Mean	2.5×10^{-3}	1.5×10^{-4}	3.3×10^{-5}	7.2×10^{-5}	1.5×10^{-5}	8.8×10^{-6}
Mode	4.0×10^{-3}	2.0×10^{-4}	1.0×10^{-4}	2.0×10^{-4}	2.5×10^{-5}	4.0×10^{-5}

Table 5. Static Stability Parameters in the Free Troposphere

Parameter	N^2, rad^2 s^{-2}			N_v^2, rad^2 s^{-2}		
Δz, m	10	100	1000	10	100	1000
Mean	1.6×10^{-4}	1.6×10^{-4}	1.7×10^{-4}	1.5×10^{-4}	1.5×10^{-4}	1.6×10^{-4}
Median	1.1×10^{-4}	1.3×10^{-4}	1.6×10^{-4}	1.1×10^{-4}	1.2×10^{-4}	1.5×10^{-4}
Mode	5.0×10^{-5}	7.5×10^{-5}	1.3×10^{-4}	7.5×10^{-5}	7.5×10^{-5}	1.5×10^{-4}

Table 6. Static Stability Parameters in the Boundary Layer

Parameter	N^2, rad^2 s^{-2}			N_v^2, rad^2 s^{-2}		
Δz, m	10	100	1000	10	100	1000
Mean	2.0×10^{-4}	2.0×10^{-4}	2.0×10^{-4}	1.8×10^{-4}	1.9×10^{-4}	1.9×10^{-4}
Median	1.0×10^{-4}	1.0×10^{-4}	1.8×10^{-4}	8.8×10^{-5}	8.8×10^{-5}	1.6×10^{-4}
Mode	7.5×10^{-5}	2.5×10^{-5}	1.0×10^{-4}	5.0×10^{-5}	2.5×10^{-5}	1.0×10^{-4}

Table 7. Percentage of Data With N^2 and N_v^2 Values ≤ 0

Parameter	N^2			N_v^2		
Δz, m	10	100	1000	10	100	1000
Free Troposphere	26	7.4	0.061	26	6.9	0.020
Boundary Layer	37	19	1.0	38	21	1.4

Table 8. Dynamic Stability Parameters in the Free Troposphere

Parameter	Ri			Ri_v		
Δz, m	10	100	1000	10	100	1000
Mean	2.6	9.7	74	2.3	9.4	75
Median	0.17	0.96	4.6	0.16	0.92	4.4
Mode	0.0	0.35	2.05	0.0	0.35	1.9

Table 9. Dynamic Stability Parameters in the Boundary Layer

Parameter	Ri			Ri_v		
Δz, m	10	100	1000	10	100	1000
Mean	6.0	7.8	120	6.5	6.2	94
Median	0.022	0.54	4.1	0.020	0.46	3.7
Mode	0.0	0.050	1.1	0.0	0.050	1.1

Table 10. Percentage of Data With Ri and Ri_v Values $\leq 1/4$

Parameter	Ri			Ri_v		
Δz, m	10	100	1000	10	100	1000
Free Troposphere	56	12	0.030	57	12	0.033
Boundary Layer	78	30	0.37	78	34	0.44

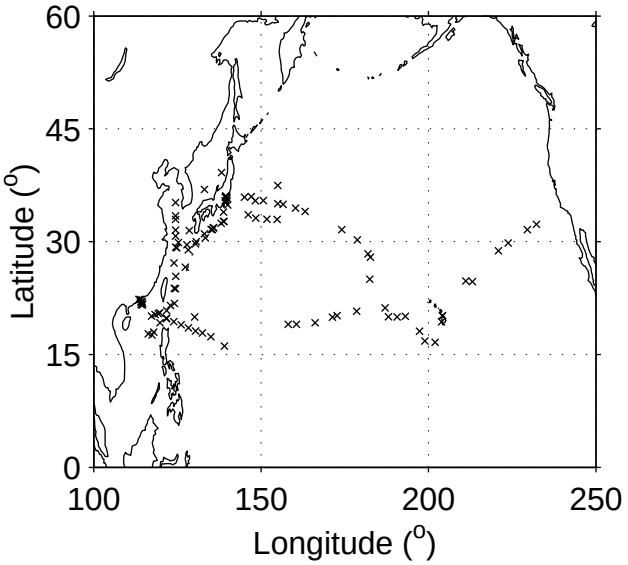
60
45
30
15
0
Latitude (o)
100
150
200
250
Longitude (o)

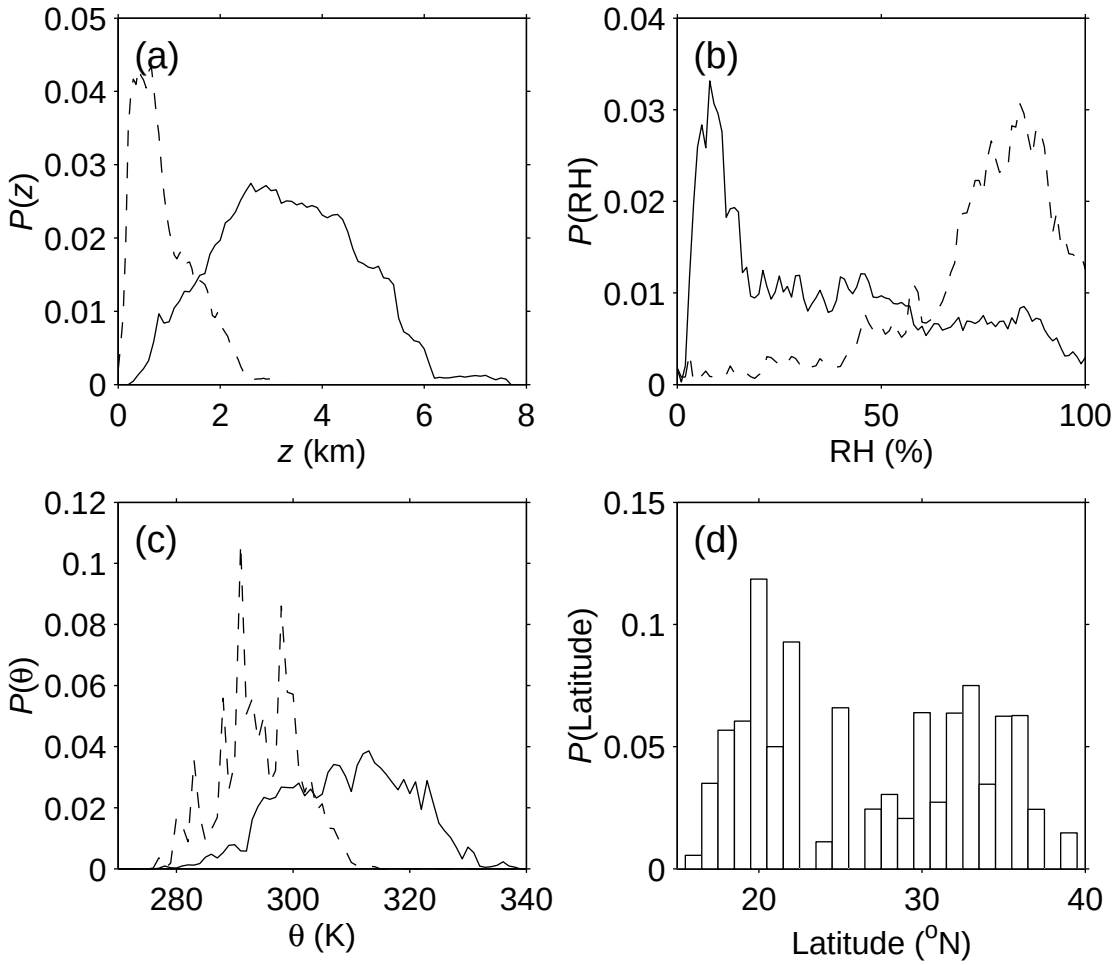
(a)
P(z)
z (km)
0.05
0.04
0.03
0.02
0.01
0
0
2
4
6
8
(b)
P(RH)
RH (%)
0.04
0.03
0.02
0.01
0
0
50
100
(c)
P(θ)
θ (K)
0.12
0.1
0.08
0.06
0.04
0.02
0
280
300
320
340
(d)
P(Latitude)
Latitude (°N)
0.15
0.1
0.05
0
20
30
40

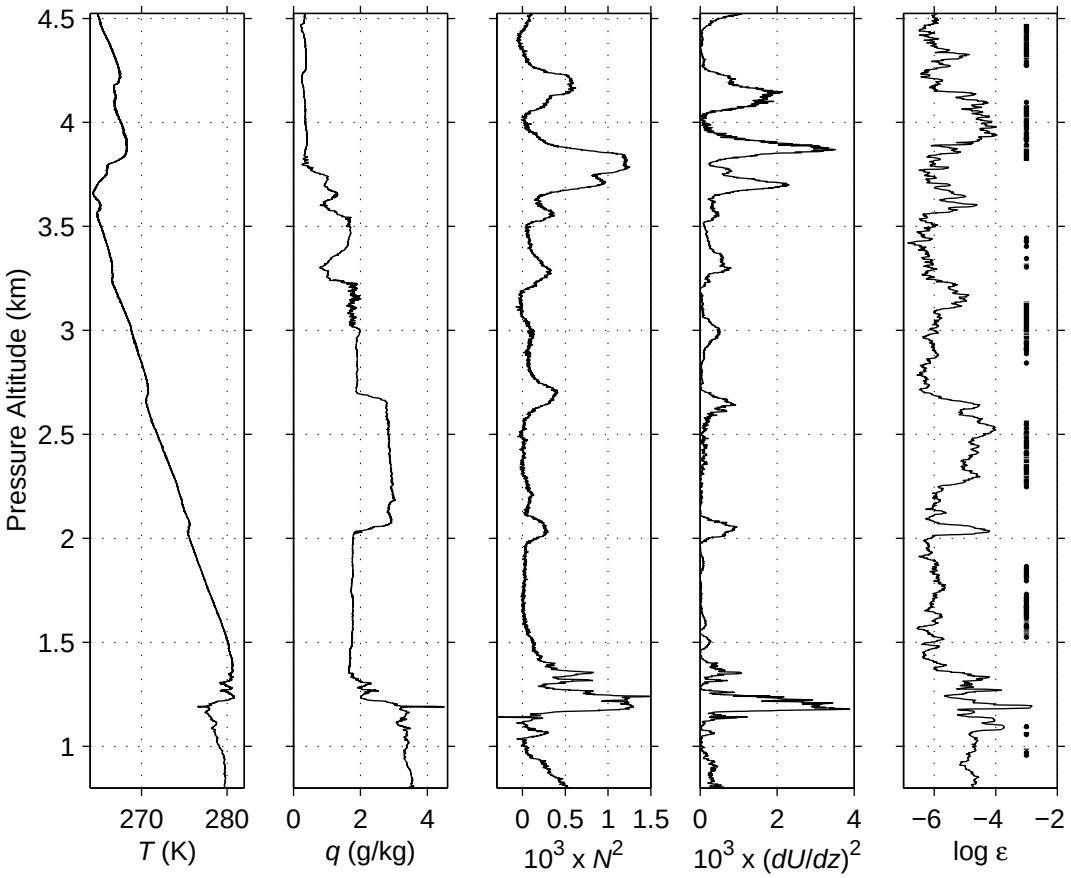
Pressure Altitude (km)
4.5
4
3.5
3
2.5
2
1.5
1
270
280
T (K)
0
2
4
q (g/kg)
0
0.5
1
1.5
10^3 x N^2
0
2
4
10^3 x (dU/dz)^2
−6
−4
−2
log ε

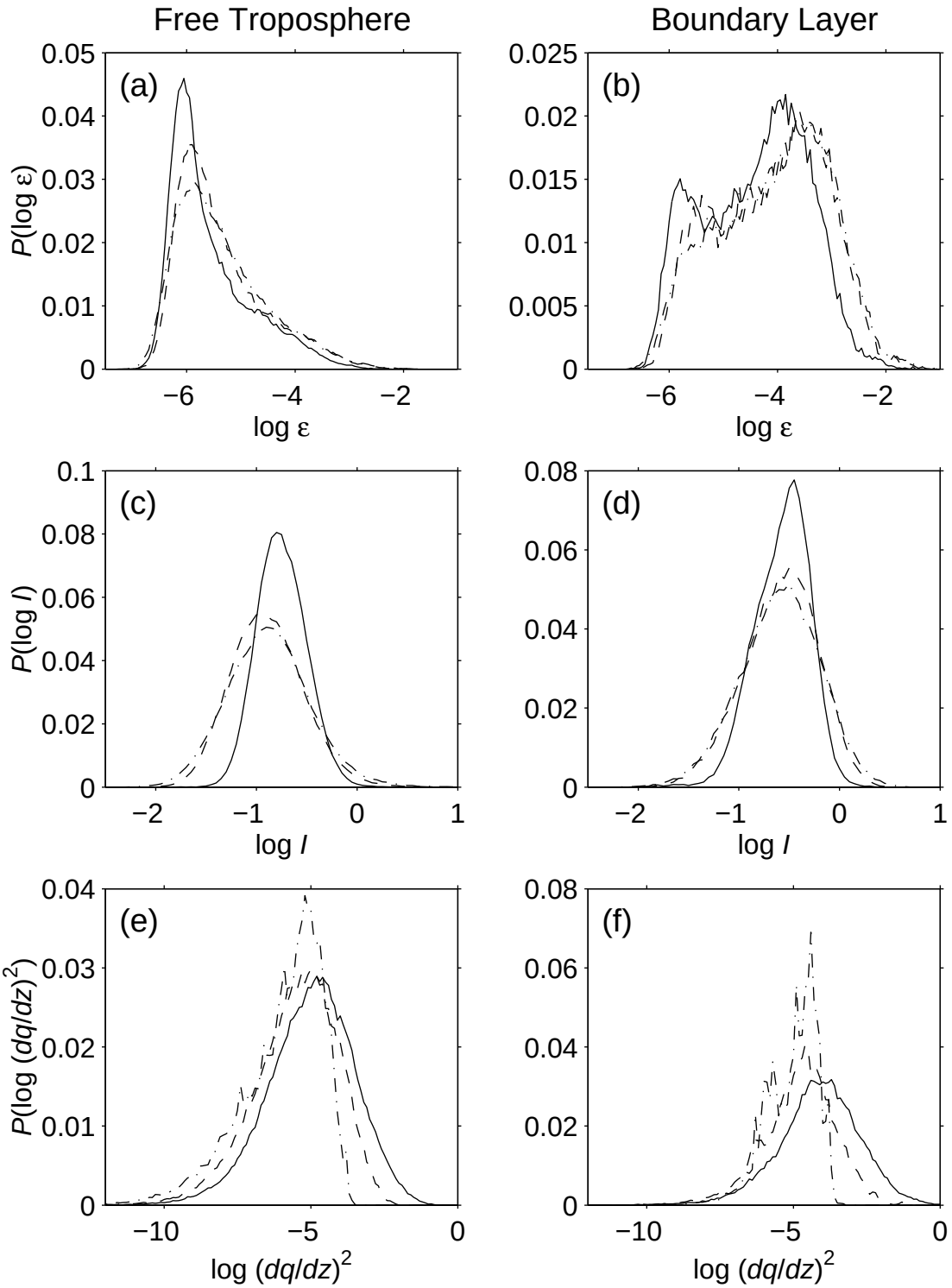
Free Troposphere
Boundary Layer
(a)
(b)
(c)
(d)
(e)
(f)
P(log ε)
log ε
P(log I)
log I
P(log (dq/dz)^2)
log (dq/dz)^2
0.05
0.04
0.03
0.02
0.01
0
0.025
0.015
0.005
0.1
0.08
0.06
0.04
0.02
−6
−4
−2
−2
−1
0
1
−10
−5

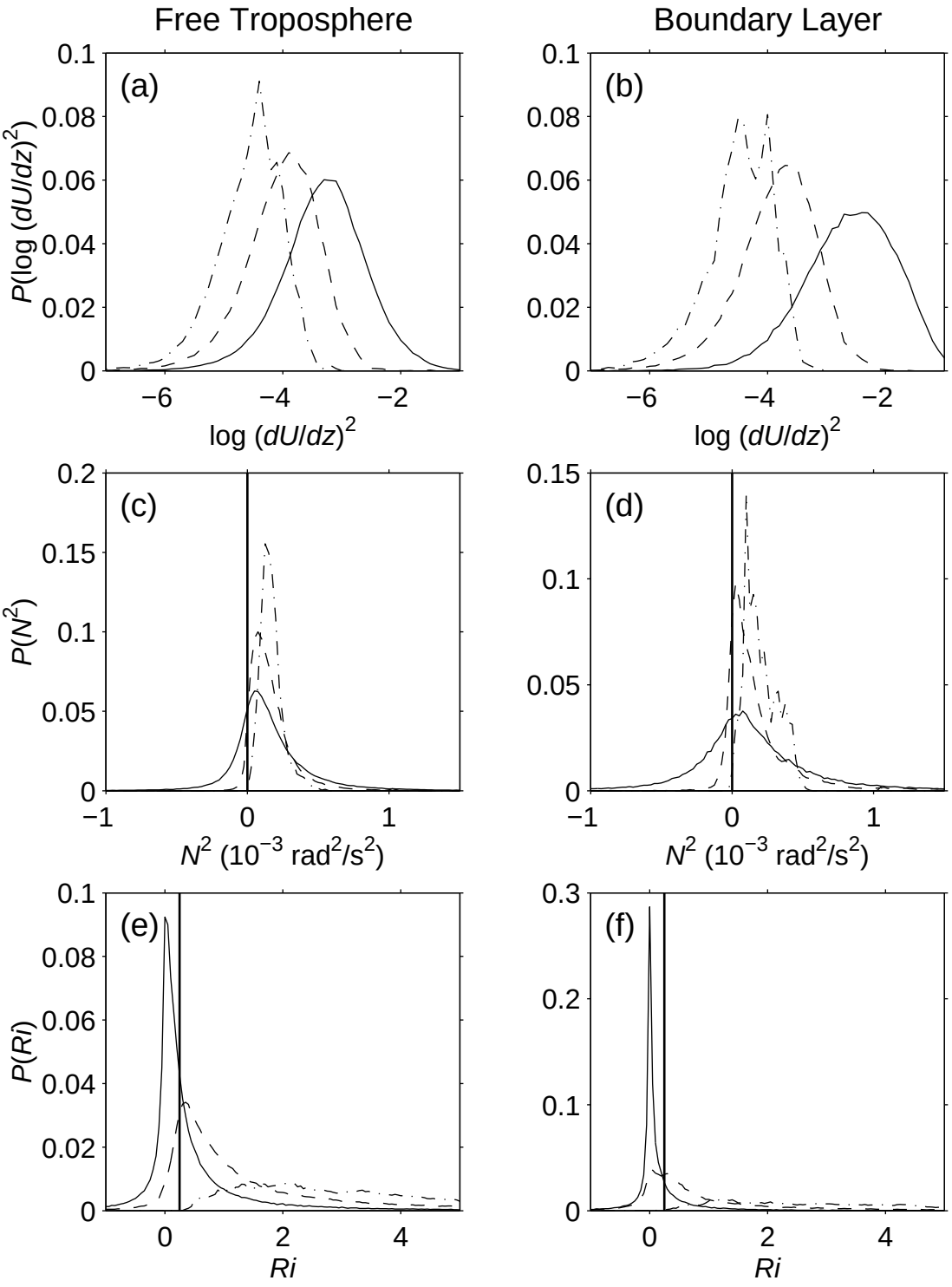
Free Troposphere
Boundary Layer
(a)
(b)
(c)
(d)
(e)
(f)
P(log (dU/dz)^2)
log (dU/dz)^2
P(N^2)
N^2 (10^−3 rad^2/s^2)
P(Ri)
Ri
0.1
0.08
0.06
0.04
0.02
0
−6
−4
−2
0.2
0.15
0.05
−1
1
0.3
2
4

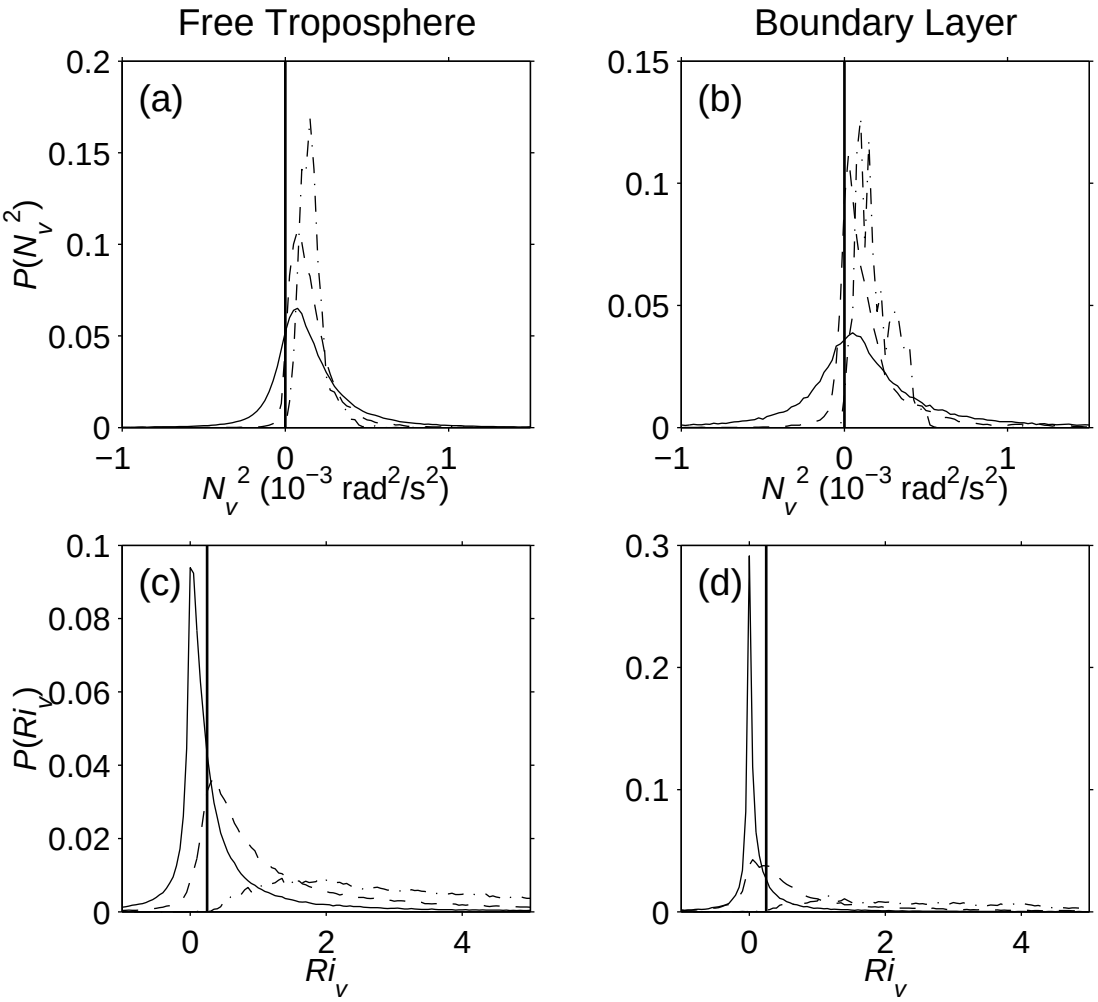
Free Troposphere
Boundary Layer
(a)
(b)
(c)
(d)
$P(N_v^2)$
N_v^2 (10^{-3} rad^2/s^2)
$P(Ri_v)$
Ri_v
0.2
0.15
0.1
0.05
0
−1
1
0.08
0.06
0.04
0.02
2
4
0.3

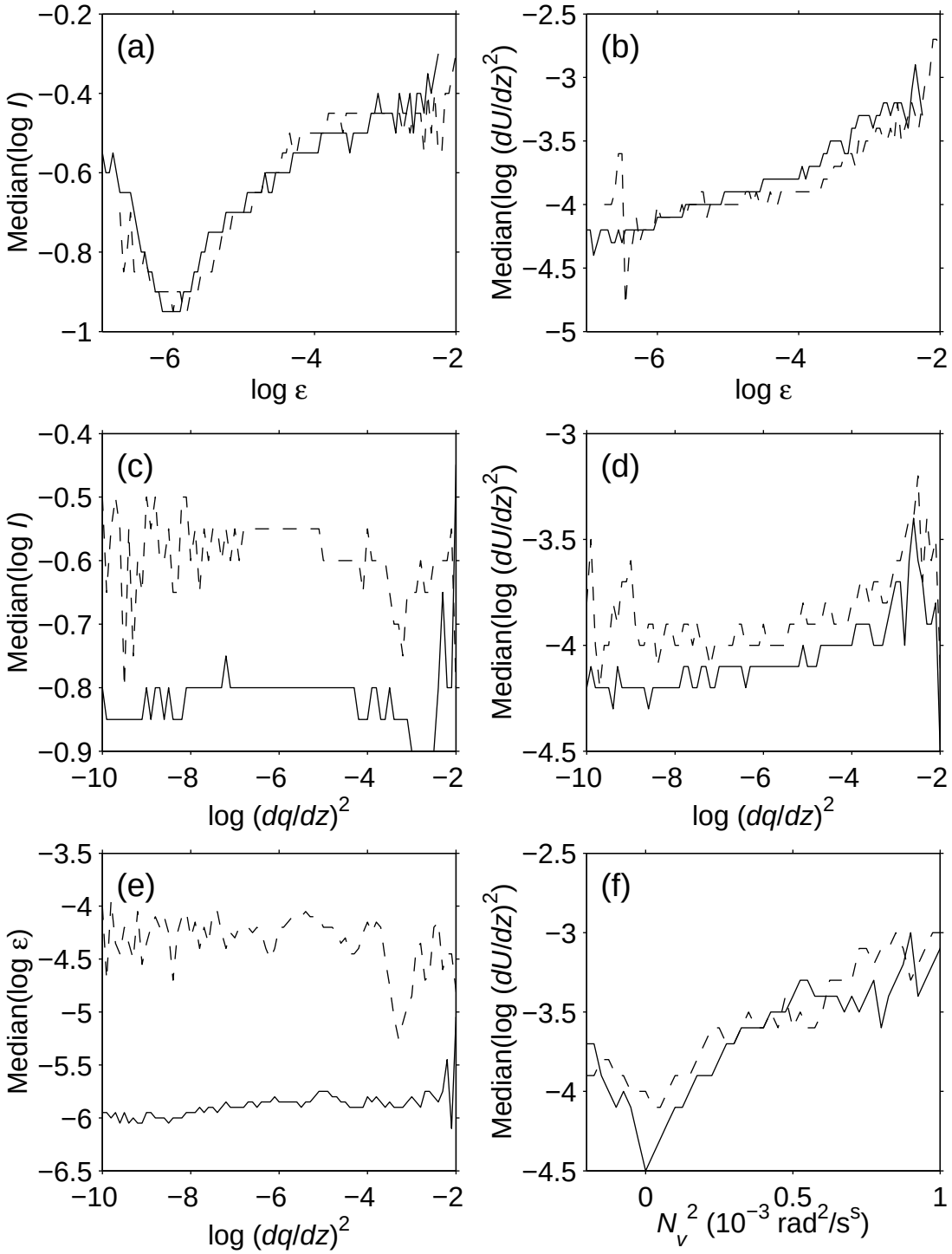
(a)
Median(log I)
log ε
(b)
Median(log $(dU/dz)^2$)
log ε
(c)
Median(log I)
log $(dq/dz)^2$
(d)
Median(log $(dU/dz)^2$)
log $(dq/dz)^2$
(e)
Median(log ε)
log $(dq/dz)^2$
(f)
Median(log $(dU/dz)^2$)
N_v^2 (10^{-3} rad^2/s^s)

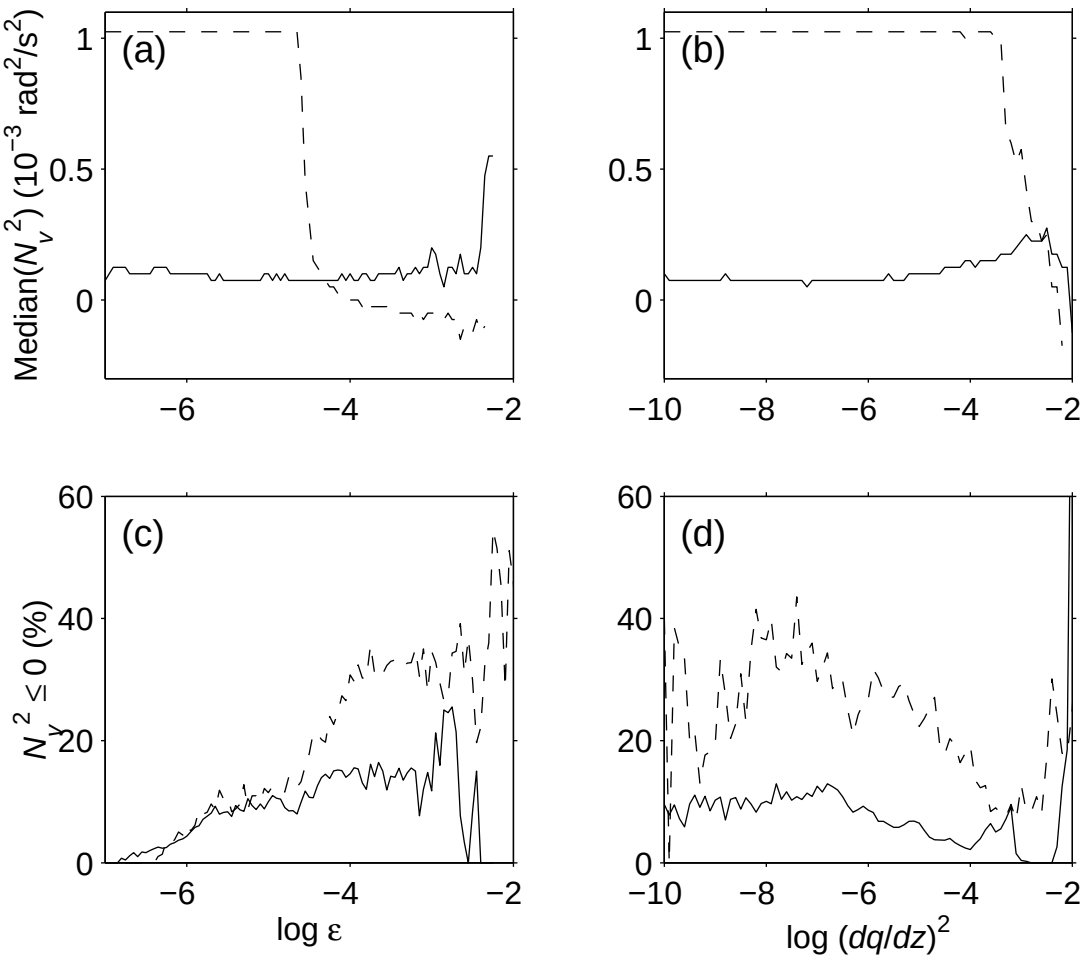
(a)
(b)
(c)
(d)
Median(N_v^2) (10^{-3} rad^2/s^2)
$N_v^2 \leq 0$ (%)
log ε
log $(dq/dz)^2$
1
0.5
0
−6
−4
−2
−10
−8
60
40
20

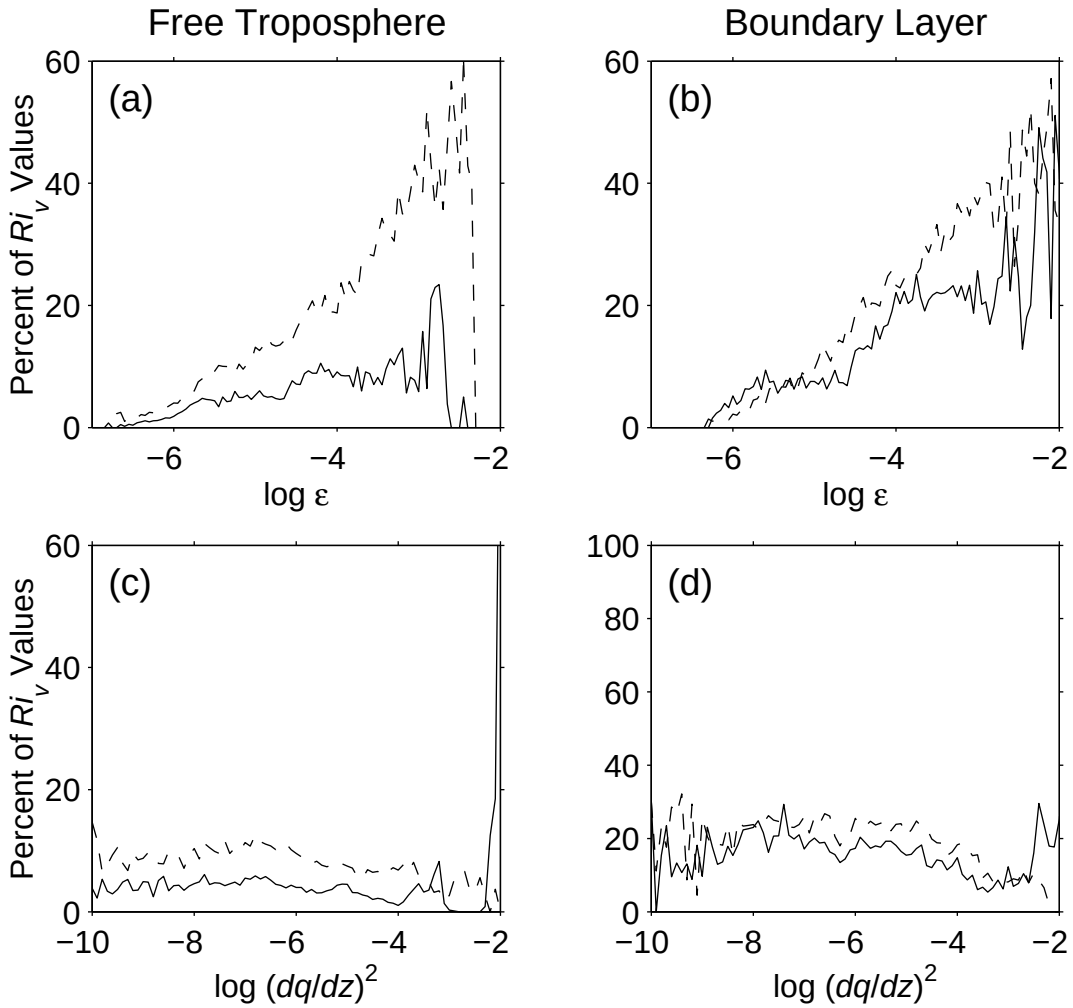
Free Troposphere
Boundary Layer
(a)
(b)
(c)
(d)
Percent of Ri_v Values
log ε
log $(dq/dz)^2$
60
40
20
0
100
80
−10
−8
−6
−4
−2